One dimensional semiconductor nanostructures: An effective active-material for terahertz detection

Miriam S. Vitiello' , Leonardo Viti, Dominique Coquillat, Wojciech Knap, Daniele Ercolani, and Lucia Sorba

Citation: APL Materials **3**, 026104 (2015); doi: 10.1063/1.4906878
View online: http://dx.doi.org/10.1063/1.4906878
View Table of Contents: http://aip.scitation.org/toc/apm/3/2
Published by the American Institute of Physics

One dimensional semiconductor nanostructures: An effective *active*-material for terahertz detection

Miriam S. Vitiello,[1,a] Leonardo Viti,[1] Dominique Coquillat,[2] Wojciech Knap,[2] Daniele Ercolani,[1] and Lucia Sorba[1]
[1]*NEST, Istituto Nanoscienze—CNR and Scuola Normale Superiore, Piazza San Silvestro 12, Pisa I-56127, Italy*
[2]*Laboratoire Charles Coulomb (L2C), UMR 5221 CNRS-University Montpellier 2, Montpellier, France*

(Received 9 December 2014; accepted 16 January 2015; published online 17 February 2015)

One-dimensional (1D) nanostructure devices are at the frontline of studies on future electronics, although issues like massive parallelization, doping control, surface effects, and compatibility with silicon industrial requirements are still open challenges. The recent progresses in atomic to nanometer scale control of materials morphology, size, and composition including the growth of axial, radial, and branched nanowire (NW)-based heterostructures make the NW an ideal building block for implementing rectifying diodes or detectors that could be well operated into the Terahertz (THz), thanks to their typical achievable attofarad-order capacitance. Here, we report on our recent progresses in the development of 1D InAs or InAs/InSb NW-based field effect transistors exploiting novel morphologies and/or material combinations effective for addressing the goal of a semiconductor plasma-wave THz detector array technology. Through a critical review of *material*-related parameters (NW doping concentration, geometry, and/or material choice) and *antenna*-related issues, here we underline the crucial aspects that can affect detection performance across the THz frequency region. [http://dx.doi.org/10.1063/1.4906878]

Terahertz (THz) radiation, loosely defined as the 30-300 μm wavelength region, lies in the electromagnetic spectral window defined for a long while as "THz gap," due to the lack of compact, solid-state, coherent radiation sources as well as fast, sensitive, and low-noise detectors.

In the last decade, from several perspectives, materials research has played an essential role in "filling" this gap. As a major example, the issue of THz generation has started to be seriously addressed with the development of THz quantum cascade lasers (QCLs),[1] relying heavily on semiconductor heterostructured artificial nano-materials. On the other hand, the development of novel THz spectroscopy,[2] nano-spectroscopy[3] and THz imaging[4–6] provided a powerful tool for the characterization of a broad range of materials, including one-dimensional (1D) or two dimensional (2D) semiconductors,[2,3] biomolecules,[7] and graphene.[8] The development of a complementary detection technology remains one of the top scientific priorities to fulfill THz application-oriented needs in fields as biomedical diagnostics, security, cultural heritage, quality and process controls,[9] high data rate wireless communication,[10,11] requiring *ad hoc* integrated generation/detection systems.

THz and sub-THz detection systems can be classified into two main categories:[12] (i) incoherent detection systems (with direct detection sensors), which are only sensitive to signal amplitude and which, as a rule, are inherently broadband; (ii) coherent detection systems, which allow simultaneously detecting signal amplitude and phase and that are inherently selective (narrow-band).

Coherent detection is conventionally achieved via heterodyne systems in which the detected signals are transferred, via mixers, to much lower frequencies (10-30 GHz) and then amplified.

[a]E-mail: miriam.vitiello@sns.it

Frequently used mixers are devices having a strong electric field quadratic nonlinearity as forward-biased Schottky barrier diodes (SBDs), superconductor-insulator-superconductor (SIS) tunnel junctions, semiconductor and superconducting hot electron bolometers (HEBs) and superlattices (SLs).[12] Clear advantages of heterodyne detection techniques are the possibility to be sensitive on both frequency modulation and phase modulation, the negligible sensitivity to background radiation noise (usually dominant in the THz), and the possibility to detect much weaker radiant signal powers compared to direct detection. Clear disadvantages are the need of equally polarized, coincident, and identical diameter beams and the difficulty to produce large format arrays.

Incoherent THz detectors nowadays employed for applications are based on thermal sensing elements that are either very slow (10-400 Hz modulation frequency for Golay cells or pyroelectric elements, with noise equivalent powers (NEPs) in the 10^{-10} $WHz^{-1/2}$ range)[12] or require deep cryogenic cooling (4 K for superconducting Nb or NbN based hot-electron bolometers), while those exploiting fast non-linear electronics (Schottky diodes) show a dramatic drop of their performance at frequencies larger than 1 THz.[13] Recently, electronic devices based on the gate-modulation of the conductance channel by the incoming radiation have been realized in high-electron-mobility transistors, field effect transistor (FETs), and metal-oxide-semiconductor FET architectures either in single-pixel[14,15] or multi-pixel focal-plane array configurations[16] exploiting different material systems including Si, GaAs/AlGaAs, InGaP/InGaAs/GaAs, and GaN/AlGaN.[12]

More recent research activities in the field of THz detectors focus on the development of detection technologies exploiting novel materials to improve specific detection figures of merit. As an example, photoemissive detectors based on AlGaAs and GaSb structures or GaAs/AlGaAs modulation doped structures have been proposed and realized although with quite low quantum efficiencies in the THz;[12] also, photothermoelectric detectors based on carbon nanotubes embedded in a *p-n* junction were successfully implemented with reasonably high responsivity (a few V/W) in the $\nu > 1$ THz frequency range.[17]

We recently proposed 2D- or 1D-FETs based on graphene[18–20] or semiconductor nanowires (NWs)[21–25] as a low-noise, high speed, and high efficiency detection technology across the THz band. Our architecture strategy is based on the possibility to engineer the channel of a FET as a resonator for plasma waves, whose frequency can be properly tailored across the THz: gated regions hundreds-nm wide can indeed support propagation of collective density oscillations (plasma waves) at THz frequencies. Under these conditions[26] when a THz wave modulated at specific frequencies (*ac*) is funneled onto the channel of a FET, it modulates the gate (G) and source (S)-drain (D) potentials, generating a continuous (*dc*) source-drain voltage Δu (or current Δi), which can be maximized by varying the gate bias V_G. The photovoltage (or photocurrent) response of the electron system in the FET, that is, the electric potential difference between D and S, contains a *dc* component even if the incoming field is *ac* and thus provides rectification of the signal. Rectification can here occur as an effect of the nonlinear response of the electron gas in the FET channel and is unrelated to extrinsic rectification mechanisms due to Schottky barriers at contacts or other circuital elements that respond in a non-ohmic manner.

The related induced excitation of plasma oscillations can either propagate in the channel (plasma-waves regime)[26] or be damped (overdamped plasma waves).[26] In the first case, a strong resonant photoresponse is achieved, and channel materials having plasma damping rates lower than both the frequency of the incoming radiation and the inverse of the wave transit time in the channel are usually needed. This condition requires channel material mobility (μ) of at least several thousand cm^2/Vs at frequencies >1 THz. In the second case, when plasma oscillations are overdamped, i.e., decay on a distance smaller than the channel length, broadband THz detection is predicted to occur.[26] In such a ballistic regime, the diffusive model of transport applies and Δu is proportional to the gate-induced conductivity (σ) change, meaning that very large transistor transconductances (G_m) can allow larger signal to noise ratios and higher efficiency response. Moreover, the gated region width, x, plays a fundamental role in increasing the photo-induced voltage,[26] being

$$\Delta u \propto \left[1 - \exp\left(\frac{-2x}{l}\right)\right], \tag{1}$$

where the decay distance $l = s\left(\frac{2\tau}{\omega}\right)^{1/2}$ depends of the incoming angular frequency ω and the momentum relaxation time τ. In a more general picture, one can write

$$\Delta u \propto U_a{}^2 \frac{1}{\sigma} \frac{d\sigma}{dV_G}, \tag{2}$$

where U_a is the amplitude of the radiation-induced modulation of the S-to-G voltage. In the low frequency regime ($\omega\tau \ll 1$), Eq. (2) becomes

$$\Delta u = \frac{U_a{}^2}{4U_0}, \tag{3}$$

where the voltage swing $U_0 = U - V_{th} = Q/C_{wG}$ being C_{wG} the electrical capacitance between the channel and the gate, V_{th} the threshold voltage and Q the channel carrier concentration. In practical devices, Δu should be divided by an additional factor $(1+R/Z)$, where R is the channel resistance and Z is the complex load impedance including the load resistance R_L, the preamplifier impedance R_{IN}, and the overall parasitic capacitances C, i.e., $\frac{1}{Z} = \frac{1}{R_{IN}} + \frac{1}{R_L} + i\omega C$.

Regardless the operating regimes, some asymmetry between S and D is needed to induce Δu; this usually stems from the asymmetry in feeding the incoming radiation, which can be achieved either by using a special antenna or by an asymmetric design of S and D contacts or even engineering an anti-symmetric channel.

Recently, we developed antenna coupled InAs NW-FETs THz detectors operating in the overdamped regime.[21–24] InAs NWs, with narrow bandgap and degenerate Fermi-level pinning, revealed to be a successful material choice for preserving good detecting performances while scaling down the dimension of the device to increase the detected frequency up to the 1.5-3 THz range, accessible with QCL sources.[22]

In this paper, we report on our recent progresses in engineering 1D NW FETs exploiting novel materials combinations and/or geometries to address simplified architectures and fast response times, beneficial for addressing the goal of a semiconductor plasma wave detector array technology.

The sub-micron size of a semiconductor NW is ideal to "design" specific functionalities in a FET: NWs can be assembled with specific compositions, heterojunctions, and architectures, promising advanced performance at dimensions compatible with on-chip technologies; they also offer significant flexibility in engineering desired transport and optical device properties, mainly due to the extremely precise control of the chemical, geometric, and electronic characteristics that can be tailored on purpose during the growth process. Furthermore, the flexibility to be easily removed from the host substrate and placed on the top of a specifically selected material for individual contacting, even in relatively large numbers, with a simple planar technology makes NWs very suitable for low capacitance circuits.[27]

There are several factors that can play a dominant role in the detection performance of a one-dimensional NW-based FET. In this letter, we critically review some *material*-related parameters (NW doping concentration, geometry, and/or material choice) and *antenna*-related matters.

In this perspective, we fabricated a set of FETs exploiting self-assembled semiconductor NWs based on different material systems/morphological conditions, obtained through specifically optimized growth settings. In all cases, ≈1.5-2 μm long NWs were grown bottom-up by chemical beam epitaxy in a Riber Compact-21 system, via Au-assisted growth using trimethylindium (TMIn) and tertiarybutylarsine (TBAs) as metal-organic (MO) precursors.[28] Before initiating the growth, the samples were heated at 500 °C under TBAs flow for 20 min. The temperature was then lowered to the growth temperature (410 °C) and to grow the InAs NWs. For *n*-type doping during the growth, we used ditertiarybutyl selenide (DtBSe) as selenium source with a controlled line pressure. *Se*-doping can be used both to control the charge density in the NW and to optimize source-drain and contact resistances when the NW is implemented in a 1D FET, while ensuring sharp pinch-off in the FET transconductance.

Fig. 1(a) shows the scanning electron micrograph image of a forest of 40 nm diameter InAs NWs. In previous works, through the systematic characterization of both the transconductances normalized to the G width w_G ($g_m = G_m/w_G$) and the resistivity (ρ) in a set of InAs FETs (Fig. 1(b)),[28] we have demonstrated that to optimize the device transport properties, a compromise

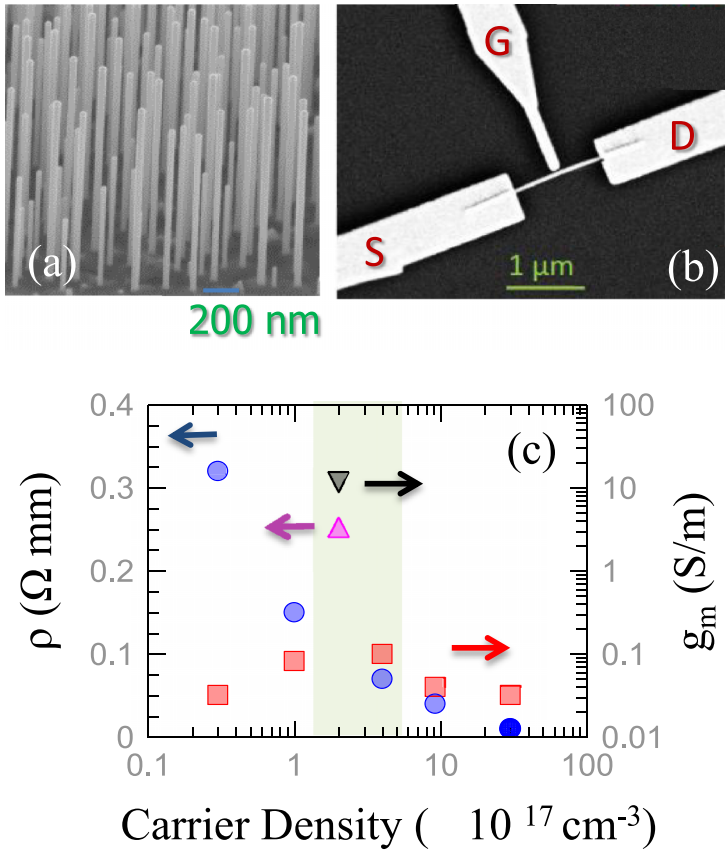

FIG. 1. (a) 45° tilted scanning electron micrograph (SEM) image of a forest of InAs nanowires having a length of about 1.5 μm, an average diameter 2r = 35 nm, and grown with DtBSe precursor line spressures of 0.1 Torr. (b) SEM image of a FET based on an InAs NW. (c) Peak transconductance (red squares) normalized to the gate length (g_m) and resistivity (ρ). Values are plotted as a function of extracted carrier density in the transistor channel; the black and pink triangles correspond to the g_m and ρ values of device A.

should be found between high G_m and sufficiently low ρ. As shown in Figure 1(c), by playing with the DtBSe line pressure, we found an ideal good trade-off when $G_m/w_G \approx 0.1$ S/m and, simultaneously, $\rho = 0.05\ \Omega$ mm, corresponding to a carrier density value

$$n = \frac{C_{wG}V_{th}}{w_G e\pi r^2} \tag{4}$$

approaching 4×10^{17} cm^3, homogeneously distributed along the section of a NW having an average diameter $2r = 35$ nm.[28] Here the NW-gate capacitance is estimated as: $C_{wG} = C_{tot} - C_{electrodes}$, being C_{tot} the capacitance between G and the whole conductor formed by S, D, and the NW itself and $C_{electrode}$ the capacitance between G and the other electrodes without NW, as schematically shown in Fig. 2(a).

Such an approach has been successfully exploited to develop THz FET detectors in the overdamped plasma wave regime, operating between 0.3 and 1.5 THz with responsivities up to ≈12 V/W and noise equivalent powers NEP = 6×10^{-11} W/√Hz by employing either *bow-tie*[22] or *log-periodic*,[21] antennas. The lower bound of the spectral band of such antennas corresponds to a wavelength that is twice the overall antenna length. In all cases, our antennas have been designed in a geometrical matching with the wavelength of the incoming beam, i.e., exploiting the relation $\lambda = 2L$, where L is the length of an individual bow. We here fixed $w_G = 100$ nm to keep the parasitic capacitance C_{SG} between S and G below 75 aF. The resulting $C_{wG} = 23$ aF could be estimated by employing the so-called *metallic approximation*. The latter assumes that the electrostatic potential cannot penetrate inside the NW, whose surface behaves like a metallic layer.[29] This simplified

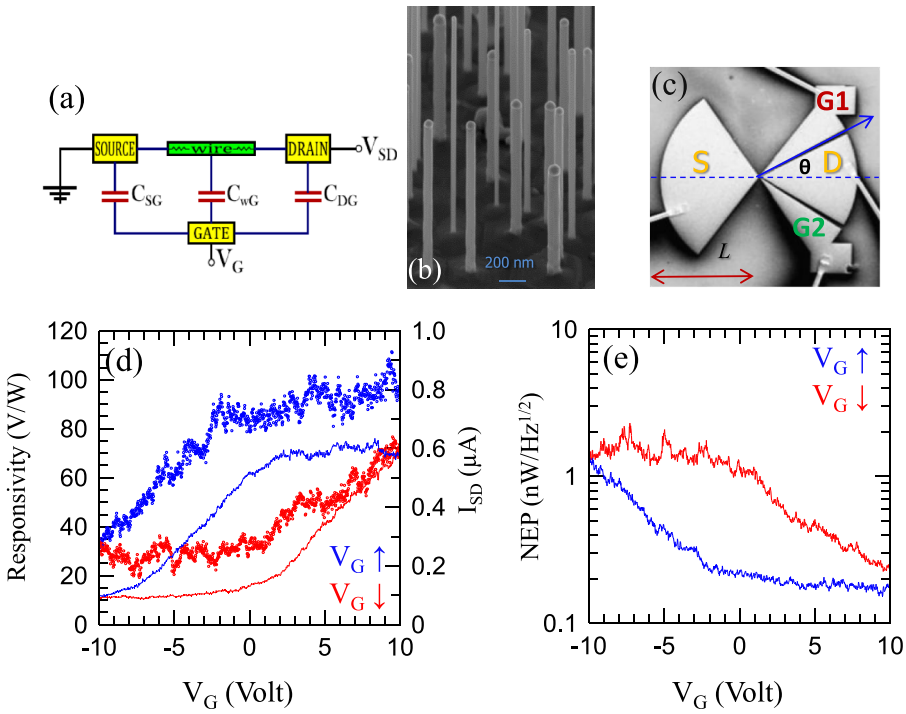

FIG. 2. (a) Equivalent *dc* circuit of a NW FET; (b) 45° tilted SEM image of a forest of InAs nanowires having a length of about 1.5 μm, an average diameter 2r = 80 nm, and grown with DtBSe precursor line pressure of 0.05 Torr. (c) SEM image of the FET based on an InAs NW and a split bow-tie antenna, having the individual bow-length L = 0.5 mm; the source (S), drain (D), and gate (G) electrodes are labeled on the image. The dashed line indicates the direction of the polarization of the incoming THz wave. (d) Responsivity (curves in dots) of the NW FET to the radiation of a 0.29 THz electronic source, modulated at 473 Hz, as a function of the gate voltage measured at T = 300 K and at zero applied V_{ds} while the polarization of the incoming beam is parallel with respect to the bow-tie antenna axis and while increasing (blue dots) or decreasing (red dots) the gate bias. The right vertical axis (continuous curves) shows the corresponding current-voltage (I_{ds}–V_G) transfer characteristic measured at room temperature and at a drain-to-source voltage V_{ds} = 0.025 V. (e) Noise equivalent power as a function of the gate voltage measured while increasing (blue curve) or decreasing (red curve) the gate bias.

model is known to be valid for NW having $n \geq 10^{17}$ cm^{-3}, i.e., enough to screen the electrostatic potential out of the semiconductor.

It is clear that in the lateral gate 1D configuration of a NW FET, a compromise should be found between large gate widths, beneficial for higher responsivities (see Eq. (1)) and the related detrimental increase of the parasitic capacitances $C_{electrode}$. Engineering a high responsivity NW FET detector in a convenient shape suitable to address such requirements then means to find a proper "architecture" trade-off. To address this issue, following Eq. (2), we can then play with (i) the gate-induced conductivity change that is in turn related with C_{wG} (see Eq. (3)) and (ii) U_a that in turn mostly depends on the coupling efficiency of the incoming radiation to the antenna as well as on the impedance mismatch of the transistor.

By keeping constant n to the mentioned $\approx 10^{17}$ cm^3—order of magnitude trade-off condition, via a controlled DtBSe precursor line pressure sets to 0.05 Torr, we have grown InAs NW with larger radii ($2r$ = 80 ± 26 nm) (Fig. 2(b)). Such a condition corresponds to larger C_{wG} (see Eq. (4)).

The NWs were then mechanically transferred to a 350 μm thick high-resistivity Si substrate, with a 300 nm SiO_2 insulating oxide surface layer and a grid of metallic markers for the alignment of lateral gated NW-FETs in the subsequent lithographic steps. The sample was spin-coated with e-beam sensitive resist, and both contact patterns and the w_G = 80 nm lateral gate were exposed by electron beam lithography in the shape of a split bow-tie antenna structure (Fig. 2(c)) having 2L = λ and an individual bow opening angle of 115°. In the resulting device (device A), all antenna bows then act as FET electrodes; one bow is split between G and D, meaning that it simultaneously applies gate bias and acts as a separate electrode allowing read-out of the rectified signal at the *D* contact.

To electrically characterize our devices, we employed the DACs of a SR830 amplifier to drive independently the S-D bias V_{SD} and V_G. The D contact was connected to a current amplifier converting the current into a voltage signal with an amplification factor of 10^4 V/A. The latter signal was then measured with an Agilent 34401A voltmeter reader.

In the case of device A, a normalized transconductance value (12.5 S/m) was achieved (black triangle in Fig. 1(c)) almost two order of magnitude larger than that obtained in the previous devices (red squares in Fig. 1(c)). From the analysis of the transfer characteristic (I_{SD} versus V_G), we extracted[30] $\mu = G_m {w_G}^2/(C_{wG} \cdot V_{sd}) \approx 1200$ cm^2/Vs, $n = C_{wG} V_{th}/(2\pi r^2 w_G) \approx 2 \times 10^{17}$ cm^{-3}, where $C_{wG} \approx 40$ aF and consequently the electron momentum relaxation time[28] $\tau = \mu m^*/e = 13$ fs. This means that at frequencies <1 THz, device A could only operate in the low frequency regime ($2\pi\nu\tau < 1$), in which plasma waves are overdamped.

Photoresponse experiments were performed with a tunable electronic source in the 0.26-0.38 THz range. The optical beam, mechanically chopped at 473 Hz and collimated by a set of off-axis f/# = 1 parabolic mirrors, was focused in a 4 mm-diameter spot, having incident power P_t, ranging, as a function of the wavelength, between 0.34 mW and 0.26 mW. From geometrical consideration, one can infer the total electromagnetic THz power P_a impinging on the antenna. Taking into account that the total detector area is smaller than the diffraction limited one, the active area is taken equal to $S_\lambda = \lambda^2/4$; besides this, the beam spot area is given by $S_t = \pi d^2/4$ and $P_a = P_t \cdot (S_\lambda/S_t)$ = 7.1-5.6 μW.[21] The photoinduced source-drain voltage Δu was measured at the D contact, while keeping $V_{sd} = 0$ and S grounded, with a lock-in amplifier (LIA) connected to a low-noise voltage preamplifier having an input impedance of 10 MΩ and an amplification factor $G_n = 25$. Δu can be therefore estimated from the signal measured by the LIA as $\Delta u = 2.2 \cdot (\text{LIA})/G_n$, where the factor 2.2 takes into account that the lock-in gives the rms of the fundamental sine wave Fourier component of the square wave produced by the chopper. Loading effects due to the finite input impedance of the lock-in-amplifier were neglected. The responsivity R_v is then defined as the ratio between the photoresponse (Δu) and the radiation power (P_a) impinging on the active area of the device.

R_v measured at 0.29 THz for device A is reported in Fig. 2(d). Maximum $R_v = 110$ V/W significantly larger than in previous reports was found. The corresponding NEP was 2×10^{-10} W/$\sqrt{\text{Hz}}$ (Fig. 2(e)), regardless the voltage sweep direction, that causes the expected hysteretic behaviour. Such a performance is almost independent from the antenna configuration. Either a simple bow-tie[24] or a metamaterial-resonant antenna[25] indeed gave comparable responsivities when patterned asymmetrically between G and S. In agreement with previous reports,[21] no signal was detected in similar devices exploiting identical antennas patterned symmetrically between source and drain, ruling out any effect related to temperature changes or to nonlinearity of the contact junctions. Figure 3 shows the 3D plot of the angle-resolved and frequency resolved responsivity of device A. Two responsivity peaks can be identified: one located at 0.29 THz, with R_v peaks at $\theta \approx 30°$ and $\theta \approx 150°$, i.e., along the inner gate-drain lobes, and the other one at 0.32 THz, with R_v peaks at $\theta \approx 0°$ and $\theta \approx 180°$.

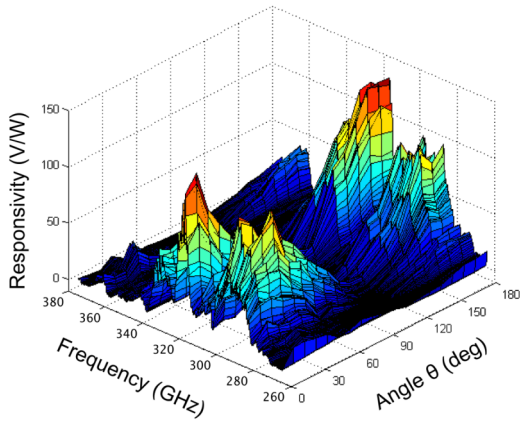

FIG. 3. Responsivity of device A measured as a function of the frequency (ν) of the electromagnetic THz wave and of the angle (θ) between the bow-tie axis and the radiation polarization vector.

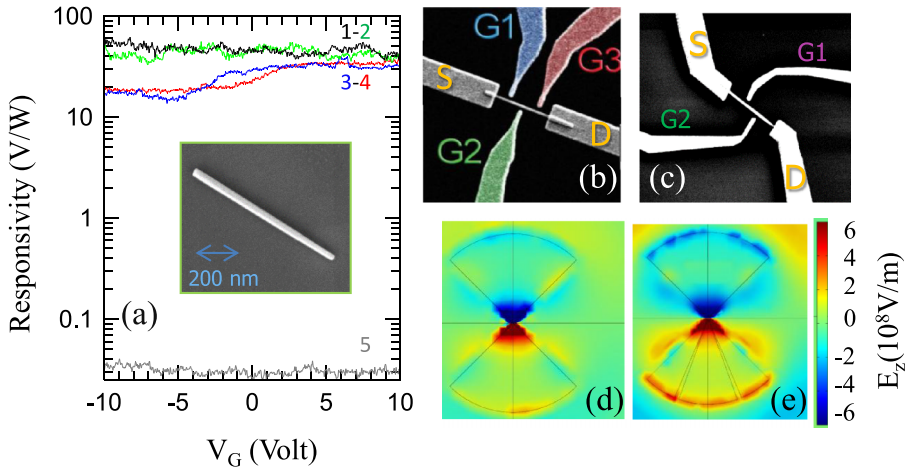

FIG. 4. (a) Responsivity to the radiation of a 0.29 THz electronic source, as a function of the gate voltage measured at T = 300 K and at zero applied V_{ds} while the polarization of the incoming beam is parallel with respect to the bow-tie antenna axis for device B (curves 1-2) exploiting a bow tie-antenna and for device C (curves 3-4) exploiting a split bow-tie antenna while increasing (1,3) or decreasing (2,4) V_g. Curve 5 represents the responsivity signal recorded in device B while switching off the THz beam. Inset: SEM image of a tapered InAs nanowire grown by applying a linear decrease in the dopant pressure from 0.4 Torr to 0 during the nanowire growth. (b) and (c) SEM image of a tapered nanowire, active element of an FET device exploiting a bow-tie (b) or a split bow tie (c) antenna: source and drain contacts of a FET are designed at the two ends of the nanowire; lateral gate electrodes were employed to determine the effect of charge density modulation on the optoelectronic properties. Gates are labeled in the direction corresponding to the doping increase, so that the highest G-label here affects the nanowire in the highest doping region; the source (S), drain (D), and gate (G) electrodes are labeled on the image. (d) and (e) Frequency domain finite element simulations of the out-of-plane electric field map of the bow tie and split bow-tie antennas, respectively, performed by using a commercial software (COMSOL Multiphysics).

As an alternative approach, we exploited the inherently asymmetric structure of tapered NWs to introduce in our FET the required asymmetry. To induce the tapered geometry, the DTBSe flow was simultaneously opened during NW growth together with TMIn and TBAs and linearly ramped down from 0.4 Torr to 0 Torr. The resulting InAs NWs show a tapering angle of 1.5° (inset Fig. 4(a)), resulting from the combined effect of low growth temperature and the presence of *Se* that reduce the adatom diffusion length leading to radial growth. The diameter of the tapered InAs varies between 68 nm and 118 nm, so that its average value approaches the NW diameter of device A.

Figure 4(a) compares the responsivity values of two FETs exploiting a bow-tie antenna patterned between S and D (Fig. 4(b), device B) (curves 1-2) or a split bow-tie antenna (Fig. 4(c), device C) (curves 3-4), both having $2L = \lambda/2$ (see Table I). Being the generated photovoltage almost independent from the position of the lateral gate,[31] we acquired our curves while polarizing simultaneously G1, G2, and G3 (Fig. 4(b)) for device B and G1 and G2 (Fig. 4(c)) for device C. The double curves 1-2 and 3-4 reflect the hysteretic behavior of the NW[19] when V_G is increased-decreased, respectively. The responsivity of device B reaches 50 V/W at 0.3 THz, independently from the applied V_G (Fig. 4(a)), making its gateless configuration with a single terminal for the rectified signal readout highly appealing for the development of a compact multi-pixel detection system. Conversely, being one antenna bow split between G and D, as an effect of the additional THz modulation at the gate-contact,

TABLE I. Morphological and geometrical values of the investigated FET devices.

Devices	NW material	Diameter $2r$ (nm)	Antenna (connections)
A	InAs	80 ± 26	Split bow-tie
B	InAs (tapered)	68–118 (on axis)	Bow-tie (S-D)
C	InAs (tapered)	68–118 (on axis)	Split bow-tie
D	InAs/InSb (tapered)	(70–110)/(120)	Bow-tie (S-D)
E	InAs/InSb (tapered)	(70–110)/(120)	Split bow-tie

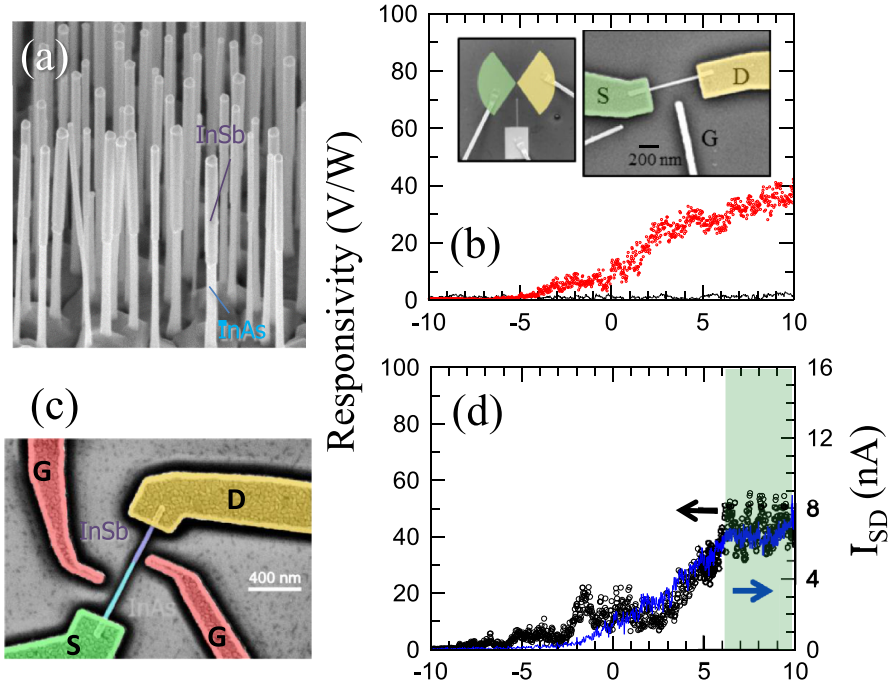

FIG. 5. (a) 45° tilted SEM image of a forest of InAs/InSb tapered heterostructured NWs having a length of about 1.2 μm. (b) Responsivity (red dots) to the radiation of a 0.3 THz electronic source, as a function of the gate voltage measured at T = 300 K and at zero applied V_{ds} while the polarization of the incoming beam is parallel with respect to the bow-tie antenna axis for device D exploiting a bow tie-antenna patterned between source (S) and drain (D) contacts. The grey curve shows the responsivity recorded in a similar device exploiting a standard un tapered InAs/InSb NW (Ref. 34) and a S-D bow-tie antenna. Insets: SEM image of the FET based on an InAs/InSb tapered NW and a bow-tie antenna, having an individual bow-length L = 0.25 mm patterned between the source (S) and drain (D) electrodes labeled on the image together with the gate pad. (c) SEM image of device E the FET is based on an InAs/InSb tapered NW and a split bow-tie antenna, having the individual bow-length L = 0.25 mm; the source (S), drain (D), and gate (G) electrodes are labeled on the image. (d) Responsivity (black dots) for device E exploiting the split bow tie-antenna to the radiation of a 0.29 THz electronic source, as a function of the gate voltage and at zero applied V_{ds} while the polarization of the incoming beam is parallel with respect to the bow-tie antenna axis. The right vertical axis (continuous blue curve) shows the corresponding current-voltage (I_{ds}–V_G) transfer characteristic measured at room temperature and at a drain-to-source voltage V_{ds} = 0.010 V.

device C shows a slightly more pronounced gate-dependent responsivity that changes by almost a factor of 2 as a function of V_G, reaching a maximum value of 35 V/W, independently from the position of the lateral gates G1 and G2 (Fig. 4(c)). For sake of comparison, the signal recorded while switching off the THz beam for device B is also shown on the graph (curve 5).

The related NEP is mostly limited by the thermal Johnson-Nyquist noise, the dominant contribution to the noise of the device, and is in the range [3×10^{-10} W/Hz$^{1/2}$–6×10^{-10} W/Hz$^{1/2}$]. Figures 4(d) and 4(e) show the frequency domain finite element (FEM) simulations of the out-of-plane electric field map of the bow-tie and split bow-tie antennas, respectively, performed by using a commercial software (COMSOL Multiphysics). In both cases, the analogous nature of dipole antenna is clearly shown, with more pronounced energy storage along the outer antenna border in the split-bow tie configuration. From the latter simulations, we estimate the complex antenna impedance whose real part approach 70 Ω for the bow-tie and reduces to 38 Ω for the split bow-tie.

We finally applied the same concept to engineer heterostructured NWs exploiting the InAs/InSb sequence and tapered along the main axis. InSb is a potentially interesting material due to its small electronic gap and high mobility. As recently demonstrated,[32–34] the InSb segment can be grown with high quality on underlying InAs stems, allowing an axial charge transport through the heterojunction, potential to achieve a further rectification effect due to band lineup. For the heterostructured InAs/InSb NWs, the InAs stem was grown by employing the same growth protocol used for the growth of tapered InAs NWs. In particular, the DTBSe flow was simultaneously opened

during the growth of InAs stem together with TMIn and TBAs and linearly ramped up from 0 Torr to 0.25 Torr, from the base of the NW to the InAs/InSb interface. Then the group-V precursor was abruptly switched from TBA to *tert*-dimethylaminoantimony (TDMASb) with a line pressure of 0.70 Torr while the TMI flux was increased to 0.45 Torr and the growth temperature was reduced by −20 °C. During the growth of the InSb segment, the DTBSe flow was continuously increased from 0.25 to 0.4 Torr from the InAs/InSb interface to the top of the NW.

Figure 5(a) shows the scanning electron microscope (SEM) image of a forest of tapered InAs/InSb NWs, showing an average tapered angle of ≈2° in the InAs segment. The latter segment has been grown under the same condition of the tapered nanowire in devices B and C.

Two FET devices (Table I) have been realized exploiting two individual tapered InAs/InSb NWs as active channel: in device D, we employ a standard bow-tie antenna patterned between S and D (SEM images in Fig. 5(b)), while device E have been fabricated with a split-bow tie antenna already illustrated in Fig. 4(c). In both cases, we fix $2L = \lambda/2$. Figure 5(b) shows the responsivity curve measured in device D as a function of V_G. Maximum responsivities of 40 V/W have been achieved. As a comparison, we here shown the responsivity curve measured in a standard InAs/InSb NW FET exploiting a symmetric S-D bow-tie antenna (grey curve).[34] As expected, as in the case of InAs,[21] no signal was detected with this symmetric antenna design (between S and D), underlining the potential of our tapered configuration to achieve the required asymmetry.

Figure 5(d) shows the transconductance characteristic and the responsivity curve measured as a function of V_G in device E (Fig. 4(c)). The responsivity and current trends are almost similar, and a maximum value of 50 V/W is here achieved, slightly larger than in device D, as an effect of the additional asymmetry induced by the antenna. For both devices D and E, the minimum NEP is 5×10^{-10} W/Hz$^{1/2}$. Comparing the results of Figs. 5(b) and 5(d) with what found in our previous works on InAs/InSb FETs exploiting an antisymmetric G-S antenna,[34] it comes out that, very differently, we here do not have any sign switch in the measured responsivity. The symmetric antenna configuration of device D, and the double-lateral gates electrode configuration of device E, helps to overcome the asymmetries of the electrical gating field induced by the presence of the single side electrode of previous devices,[34] therefore avoiding the resulting pushing/pulling of the majority carriers towards the nanowire outer surface. Such an asymmetry demonstrated to be detrimental[34] leading to a strong modification of the charge distribution within the NW when large electric fields are applied.

In conclusion, we demonstrated that 1D FETs based on semiconductor NWs are a powerful technology to develop plasma-wave detectors that could well operate into the THz promising to rapidly impact spectroscopy and imaging applications. The versatility offered by the growth protocol and the possibility to lithographically "design" the required asymmetry, mandatory for the rectification of plasma waves in the transistor channel, either via playing with the material morphology, composition, and doping or via a proper low-impedance antenna shape, make the device concept highly appealing for the development of a compact multi-pixel detection system. The latter system promises to show even in a simple two-terminal configuration, high quantum efficiencies across the THz range. Furthermore, the inherent atto-Farad order capacitance of a NW and the related 10 THz cutoff frequency is ideal to push the detection speedup to *nanosecond* scales once a proper nano-lithographic engineering of the overall circuit parasitic capacitance is performed.

This work was partly supported by the Italian Ministry of Education, University, and Research (MIUR) through the program "FIRB-Futuro in Ricerca 2010" RBFR10LULP "Fundamental research on terahertz photonic devices," by the ANR P2N NADIA "Integrated NAno-Detectors for terahertz Applications" (ANR-13-NANO-0008), and by the European Union through the MPNS COST Action "MP1204 TERA-MIR Radiation: Materials, Generation, Detection and Applications." MSV acknowledges Alessandro Tredicucci for fruitful discussions.

[1] R. Köhler, A. Tredicucci, F. Beltram, H. E. Beere, E. H. Linfield, A. G. Davies, D. A. Ritchie, R. C. Iotti, and F. Rossi, Nature **417**, 156 (2002).

[2] B. Ferguson and X. C. Zhang, Nat. Mater. **1**, 26–33 (2002).

[3] M. Eisele, T. L. Cocker, M. A. Huber, M. Plankl, L. Viti, D. Ercolani, L. Sorba, M. S. Vitiello, and R. Huber, Nat. Photonics **8**, 841–845 (2014).

[4] C. M. Watts, D. Shrekenhamer, J. Montoya, G. Lipworth, J. Hunt, T. Sleasman, S. Krishna, D. R. Smith, and W. J. Padilla, Nat. Photonics **8**, 605–609 (2014).
[5] L. Masini, S. Meucci, J. Xu, R. Degl' Innocenti, F. Castellano, H. E. Beere, D. Ritchie, D. Balduzzi, R. Puglisi, A. Galli, F. Beltram, M. S. Vitiello, M. Cecchini, and A. Tredicucci, Laser Photonics Rev. **8**, 734–742 (2014).
[6] F. P. Mezzapesa, L. L. Columbo, M. Brambilla, M. Dabbicco, M. S. Vitiello, and G. Scamarcio, Appl. Phys. Lett. **104**, 041112 (2014).
[7] L. J. Xie, Y. Yao, and Y. B. Ying, Appl. Spectrosc. Rev. **48**, 448–461 (2014).
[8] O. Mitrofanov, W. L. Yu, R. J. Thompson, Y. X. Jiang, I. Brener, W. Pan, C. Berger, W. A. de Heer, and Z. G. Jiang, Appl. Phys. Lett. **103**, 111105 (2013).
[9] M. Tonouchi, Nat photonics **1**, 97–105 (2007).
[10] S. Blin, L. Tohme, D. Coquillat, S. Horiguchi, Y. Minamikata, S. Hisatake, P. Nouvel, T. Cohen, A. Penarier, F. Cano, L. Varani, W. Knap, and T. Nagatsuma, J. Commun. Networks **15**, 559 (2013).
[11] L. Tohmé, S. Blin, G. Ducournau, P. Nouvel, D. Coquillat, S. Hisatake, T. Nagatsuma, A. Pénarier, L. Varani, W. Knap, and J.-F. Lampin, Electron. Lett. **50**, 323 (2014).
[12] F. Sizov and A. Rogalski, Prog. Quantum Electron. **34**, 278 (2010).
[13] P. H. Siegel, IEEE Trans. Microwave Theory Tech. **50**, 910 (2002).
[14] W. Knap, M. Dyakonov, D. Coquillat, F. Teppe, N. Dyakonova, J. Lusakowski, K. Karpierz, M. Sakowicz, G. Valusius, D. Seliuta, I. Kasalynas, A. El Fatimy, Y. M. Meziani, and T. Otsuji, Int. J. Infrared Millimeter Waves **30**, 1319 (2009).
[15] A. Lisauskas, S. Boppel, J. Matukas, V. Palenskis, L. Minkevicius, G. Valusis, P. Haring-Bolivar, and H. G. Roskos, Appl. Phys.Lett. **103**, 153505 (2013).
[16] E. Ojefors, U. R. Pfeiffer, A. Lisauskas, and H. G. Roskos, IEEE J. Solid-State Circuits **44**, 1968–1976 (2009).
[17] X. He, N. Fujimura, J. M. Lloyd, K. J. Erickson, A. A. Talin, Q. Zhang, W. Gao, Q. Jiang, Y. Kawano, R. H. Hauge, F. Léonard, and J. Kono, Nano Lett. **14**, 3953–3958 (2014).
[18] L. Vicarelli, M. S. Vitiello, D. Coquillat, A. Lombardo, A. C. Ferrari, W. Knap, M. Polini, V. Pellegrini, and A. Tredicucci, Nat. Mater. **11**, 865–871 (2012).
[19] D. Spirito, D. Coquillat, S. L. De Bonis, A. Lombardo, M. Bruna, A. C. Ferrari, V. Pellegrini, A. Tredicucci, W. Knap, and M. S. Vitiello, Appl. Phys. Lett. **104**, 061111 (2014).
[20] F. H. L. Koppens, T. Mueller, Ph. Avouris, A. C. Ferrari, M. S. Vitiello, and M. Polini, Nat. Nanotechnol. **9**, 780 (2014).
[21] M. S. Vitiello, D. Coquillat, L. Viti, D. Ercolani, F. Teppe, A. Pitanti, F. Beltram, L. Sorba, W. Knap, and A. Tredicucci, Nano Lett. **12**, 96 (2012).
[22] M. S. Vitiello, L. Viti, L. Romeo, D. Ercolani, G. Scalari, J. Faist, F. Beltram, L. Sorba, and A. Tredicucci, Appl. Phys. Lett. **100**, 241101 (2012).
[23] M. Ravaro, M. Locatelli, L. Viti, D. Ercolani, L. Consolino, S. Bartalini, L. Sorba, M. S. Vitiello, and P. De Natale, Appl. Phys. Lett. **104**, 083116 (2014).
[24] L. Romeo, D. Coquillat, M. Pea, D. Ercolani, F. Beltram, L. Sorba, W. Knap, A. Tredicucci, and M. S. Vitiello, Nanotechnology **24**, 214005 (2013).
[25] L. Viti, D. Coquillat, D. Ercolani, L. Sorba, W. Knap, and M. S. Vitiello, Opt. Express **22**, 8996 (2014).
[26] M. Dyakonov and M. Shur, IEEE Trans. Electron Devices **43**, 380–387 (1996).
[27] Y. Li, F. Qian, J. Xiang, and C. M. Lieber, Mater. Today **9**(10), 18 (2006).
[28] L. Viti, M. S. Vitiello, D. Ercolani, L. Sorba, and A. Tredicucci, Nanoscale Res. Lett. **7**, 159 (2012).
[29] D. Vashaee, A. Shakouri, J. Goldberger, T. Kuykendall, P. Pauzauskie, and P. Yang, J. Appl. Phys. **99**, 054310 (2006).
[30] S. Datta, *Electronic Transport in Mesoscopic Systems* (Cambridge University Press, 1995), Chap. 1.
[31] L. Romeo, D. Coquillat, E. Husanu, D. Ercolani, A. Tredicucci, F. Beltram, L. Sorba, W. Knap, and M. S. Vitiello, Appl. Phys. Lett. **105**, 231112 (2014).
[32] P. Caroff, J. B. Wagner, K. A. Dick, H. A. Nilsson, M. Jeppsson, K. Deppert, L. Samuelson, L. R. Wallenberg, and L.-E. Wernersson, Small **4**, 878 (2008).
[33] D. Ercolani, F. Rossi, A. Li, S. Roddaro, V. Grillo, G. Salviati, F. Beltram, and L. Sorba, Nanotechnology **20**, 505605 (2009).
[34] A. Pitanti, D. Coquillat, D. Ercolani, L. Sorba, F. Teppe, W. Knap, G. De Simoni, F. Beltram, A. Tredicucci, and M. S. Vitiello, Appl. Phys. Lett. **101**, 141103 (2012).